Volume 1 | Number 1 | Jan 2013 | Pages 1–100

Nanoscale

www.rsc.org/nanoscale

ROYAL SOCIETY OF CHEMISTRY

This is an *Accepted Manuscript*, which has been through the Royal Society of Chemistry peer review process and has been accepted for publication.

Accepted Manuscripts are published online shortly after acceptance, before technical editing, formatting and proof reading. Using this free service, authors can make their results available to the community, in citable form, before we publish the edited article. We will replace this *Accepted Manuscript* with the edited and formatted *Advance Article* as soon as it is available.

You can find more information about *Accepted Manuscripts* in the **Information for Authors**.

Please note that technical editing may introduce minor changes to the text and/or graphics, which may alter content. The journal's standard **Terms & Conditions** and the **Ethical guidelines** still apply. In no event shall the Royal Society of Chemistry be held responsible for any errors or omissions in this *Accepted Manuscript* or any consequences arising from the use of any information it contains.

Enhancing UV-emissions through optical and electronic dual-function tunings of Ag nanoparticles hybridized with n-ZnO nanorods/p-GaN heterojunction light-emitting diodes

Yung-Chi Yao, [a] **Zu-Po Yang,** [*b] **Jung-Min Hwang,** [ac] **Yi-Lun Chuang,** [a] **Chia-Ching Lin,** [b] **Jing-Yu Haung,**
[a] **Chun-Yang Chou,** [a] **Jinn-Kong Sheu,** [d] **Meng-Tsan Tsai,** [e] **and Ya-Ju Lee** [*a]

ZnO nanorods (NRs) and Ag nanoparticles (NPs) are known for enhancing the luminescence of light-emitting diodes (LEDs) through high directionality of waveguide mode transmission and efficient energy transfer of localized surface plasmon (LSP) resonances, respectively. In this work, we demonstrated Ag NPs-incorporated n-ZnO NRs/p-GaN heterojunctions by facilely hydrothermally growing ZnO NRs on Ag NPs-covered GaN, in which the Ag NPs were introduced and randomly distributed on the p-GaN surface to excite the LSP resonances. Compared with the reference LED, the light-out power of the near-band-edge (NBE) emission (ZnO, λ=380 nm) of our hybridized structure is increased almost 1.5−2 times and can be further modified in a controlled manner by varying the surface morphology of the surrounding medium of the Ag NPs. The improved light-output power is mainly attributed to the LSP resonance between the NBE emission of ZnO NRs and LSPs in Ag NPs. We also observed different behavior in the electroluminescence (EL) spectra as the injection current increased for the treatment and reference LEDs. This observation might be attributed to the modification of the energy band diagram for introducing Ag NPs at the interface between n-ZnO NRs and p-GaN. Our results pave the way for developing advanced nanostructured LED devices with high luminescence efficiency in the UV emission regime.

Introduction

Zinc oxide(ZnO), due to its large exciton binding energy of 60 meV, wide direct bandgap energy of 3.37 eV, and the feasibility of growing a one-dimensional nanostructure on mismatched substrates, is one of the most promising candidates for solar cells, light-emitting diodes (LEDs), and laser diodes (LDs). Due to the intrinsic nature of n-type polarity, it is difficult to achieve stable and reproducible p-n homo-junction structures entirely made of ZnO materials; therefore, intense studies have been devoted to developing the ZnO-based p-n heterojunction structures where the ZnO material connects to other p-type materials. Among them, the n-ZnO/p-GaN heterojunction is the most common configuration in consideration of the same crystalline wurtzite structure, small lattice mismatch (~1.9%), and similar magnitude in the bandgap energy. This heterojunction structure is particularly important for LED applications and has attracted significant attention in recent years.[1-8] However, the staggered (type II) band alignment of the n-ZnO/p-GaN heterojunction inevitably causes a barrier height at the junction interface, resulting in low injected carriers that can cross the junction for electron-hole recombination, degrading the actual performances of LED devices. Recently, one-dimensional ZnO nanorods (NRs) have been implemented to improve carrier injection efficiency through nanosized heterojunctions. Additionally, the highly homogenous crystallinity inherently present in the ZnO NRs, which can be synthesized by the hydrothermal method[9-11] or other fabrication schemes,[12,13] provides excellent transportation paths for injected electrons[14] and serves as the escaping routes for trapped light to enhance the light extraction efficiency.[6,15,16] The other increasingly studied nanostructure is localized surface plasmons (LSPs) in noble metal nanoparticles (NPs). Compared to the SPs in continuous metal films,[17] LSPs are increasingly studied in metal NPs/GaN or metal NPs/ZnO-based hybrid structures due to their unique advantages, the recent improvements in NP synthesis and low cost fabrication processes.[18] In general, the most commonly used Ag and Au NPs are applied in the blue and green wavelength regions of LEDs, respectively. For example, LSP-enhanced photoluminescence (*PL*) and/or electroluminescence (*EL*) intensity was reported for Ag NPs placed on p-type GaN top layers [19,20] or embedded in n-type GaN underlying the multiple quantum-wells (MQWs) region of GaN-based LEDs. [21] In addition, LSP-enhanced *EL* intensity was demonstrated in n-ZnO/AlN/p-GaN LEDs by inserting Ag NPs between the ZnO and AlN spacer layer. [22-24] The Ag NPs were also utilized to decrease the threshold of an electrically pumped ZnO–based random laser by the LSP coupling effect. [25] The abovementioned LSP-coupling effect to enhance *PL/EL* intensity is due to the energy transition from excitons in the active region (e.g., InGaN/GaN MQWs) to LSP resonant modes of metal NPs, either through near-field coupling[26-29] (to enhance the internal quantum efficiency) or far-field coupling[30] (to enhance the light extraction efficiency), depending on the degree of spatial overlap of the extended LSP resonant modes and the exciton's wave

function (which is mainly determined by the distance of the LSP-exciton).

Although ZnO NRs and metal NPs have been recognized to have strong optical coupling effects that can enhance LED luminescence, few studies that combine these two strategies in LED devices have been reported. For instance, to enhance the ultraviolet (UV) emission of waveguide-type ZnO NRs/p-GaN heterojunction LEDs, Liu *et. al.* and Zhang *et. al.* recently utilized Ag NPs to decorate the ZnO NR's sidewall by spin-coating[31] and physical sputtering [32] methods, respectively, which are followed by an isolation process using an encapsulant package of polymethyl methacrylate (PMMA). Due to the high directionality inherent in the ZnO NRs, the generated *EL* of the LED device propagates along the axial direction of the NR's waveguide. Hence the direct interaction between the sidewall-decorated Ag LSPs and the ZnO excitons enables the *EL* to be coupled out of the NR waveguide, which is conceived as near-field optical coupling and results in an increase of the spontaneous emission rate and internal quantum efficiency of the LED device. Accordingly, the hybridization of vertically aligned ZnO NRs and metal NPs creates a frontier regime for constructing a high-efficiency LED architecture that cannot be achieved by a single nanostructure component. Nevertheless, how the Ag NPs are embedded into ZnO NRs/p-GaN interface affects the LED performance, and the mutual interactions between these two nanostructures upon such hybridized-nanostructure LED device are rarely discussed.

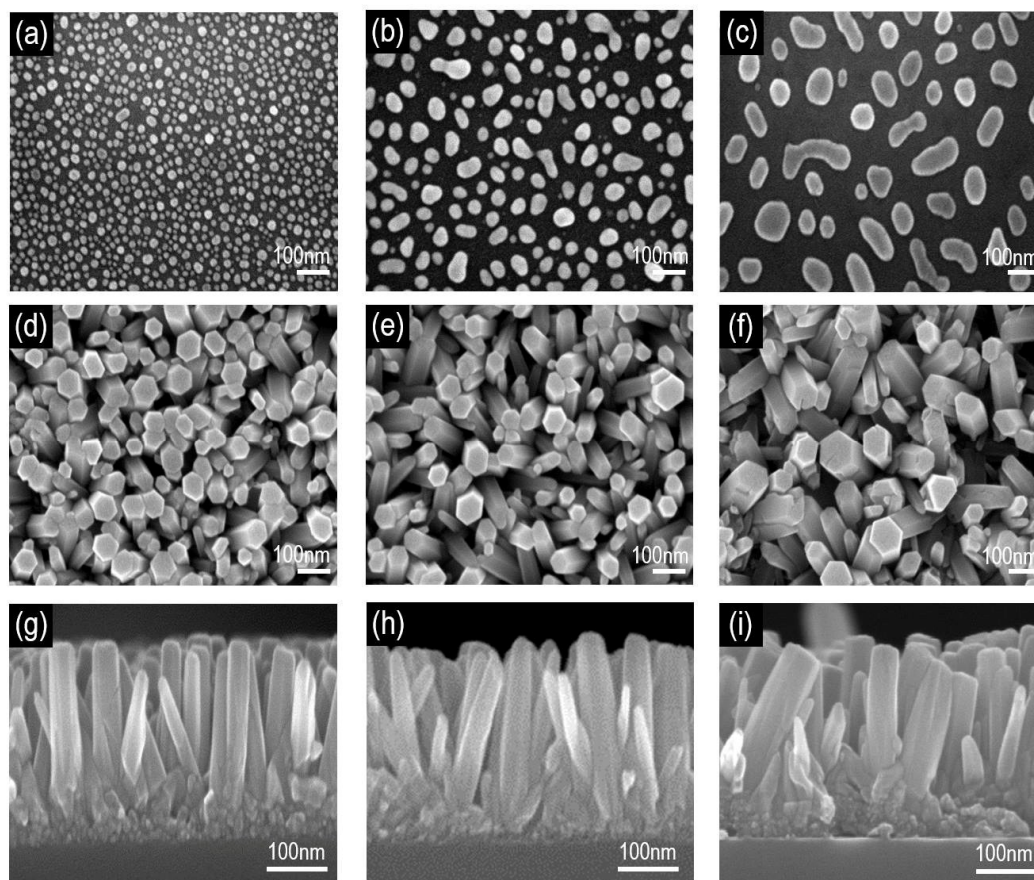In this study, we fabricated Ag NPs-incorporated

Fig. 1. Scanning electron microscope (SEM) images of self-organized Ag NPs with pre-annealed Ag film thickness of (a) 5 nm, (b) 10 nm, and (c) 15 nm. Top-view SEM images of ZnO NRs with (d) Ag NPs (5 nm), (e) Ag NPs (10 nm), and (f) Ag NPs (15 nm). The thickness of the ZnO seed layer is 30 nm for all samples. Cross-sectional SEM images to identify the synthesized length of ZnO NRs with (g) Ag NPs (5 nm), (h) Ag NPs (10 nm), and (i) Ag NPs (15 nm).

n-ZnO NRs/p-GaN heterojunctions by facilely hydrothermally growing ZnO NRs on Ag NPs-covered GaN. The Ag NPs were embedded in p-type GaN layers underlying the n-ZnO NRs region of the LED device. The ZnO NRs were interconnected by oblique-angle deposited transparent conductive films (i.e., indium-tin-oxide, ITO), which allows a direct electrical contact to the ZnO NRs and skips the PMMA isolation process generally involved in nanostructured LEDs. Few reports discussing the mechanism and performance of such hybridized type, LSP-enhanced, ZnO NRs LEDs are available. The performance of the hybridized-nanostructure LEDs was systematically examined and was found to be better than that of LEDs without incorporated Ag NPs. The observed enhancement of *PL* intensity results from the energy transfer associated with far-field optical coupling because the ZnO excitons are generated and located relatively far from the Ag NPs underneath, which is further validated by the finite-difference time-domain (*FDTD*) simulation. Furthermore, by comparing the *EL* spectra of devices with and without Ag NPs, it was found that the Ag NPs provide an additional functionality that facilitates the carrier injection by modifying the electronic band structure at interface between the n-ZnO NRs and p-GaN layer. We also discuss the possible mechanism of how Ag NPs induce the appropriate electronic band structure for the preferential near-band-edge (NBE) *EL* emission of ZnO NRs. As a result, we believe this work paves the way for developing

advanced nanostructured LED devices with high luminescence efficiency in the UV emission regime.

Experiment

5 To fabricate our Ag NPs-incorporated n-ZnO NRs/p-GaN heterojunction LED structure, a 2-µm-thick undoped GaN buffer layer and a 300-nm-thick Mg-doped GaN layer were first grown on a (0001) sapphire substrate by metal organic chemical vapor deposition (MOCVD). The hole concentration and mobility of the 10 p-type GaN layer, acquired by a four-point Hall measurement, were $p = 5.5 \times 10^{17}$ cm^{-3} and $\mu_p = 6.2$ cm^2/Vs, respectively. Thin films of Ag with different thicknesses of 5, 10, and 15 nm were deposited on the top surface of the p-GaN layer by radio frequency (RF) magnetron sputtering system followed by rapid 15 thermal annealing (RTA) treatment at 600˚C for 1 min to form self-organized Ag nanoparticles (NPs). Meanwhile, the RTA system was supplied with inert nitrogen at 500 Torr to prevent the oxidation of Ag NPs, which generally occurs in high-temperature annealing treatment. The dense cloud of inert gas molecules (N$_2$) 20 hinders the interaction of oxygen atoms with the silver surface to form silver oxide. For comparison, we also fabricated Ag NPs using the same RTA condition but in an O$_2$ atmosphere (500 Torr). The normalized absorption spectra of the Ag (5 nm) NPs fabricated by RTA treatment in N$_2$ and O$_2$ ambient environment 25 are plotted in Fig. S1 in the ESI†. No significant change in the peak intensity is observed in different ambient environment, but a clear red-shift occurred in the O$_2$ atmosphere (from 410 nm to 433 nm), which suggests the transformation of silver to silver oxide (Ag$_2$O). The red-shift of the absorption peak due to the 30 oxidation of Ag NPs decreases the degree of spectral overlap between the LSP resonance peak of the Ag NPs and the PL spectrum of ZnO NRs, which reduces the LSP enhancement of the UV emission. However, the oxidation of Ag NPs is effectively suppressed in the RTA system with N$_2$ ambient 35 atmosphere. The sample was subjected to hydrothermal treatment for the growth of ZnO nanorods (NRs). Initially, a 30-nm-thick ZnO seed layer was sputtered onto the sample's top surface followed by suspending the substrate in an aqueous solution of 400 mL zinc nitrate hexahydrate (Zn(NO$_3$)$_2$·6H$_2$O, 0.025 mol/L) 40 and 100 mL hexamethylenetetramine ((CH$_2$)$_6$·N$_4$, 0.025 mol/L) at 90 °C for 60 min in an oven. The randomly aligned ZnO NRs were then grown, and the process was finished by dipping the substrate into deionized water to remove the residual salts and drying by N$_2$ gas flow. Finally, a slanted indium-tin-oxide (ITO) 45 film with a thickness of 300 nm was grown by RF magnetron sputtering with an incident angle of $\theta = 60°$ to interconnect the ZnO Ns and to provide a continuous and conductive platform for the subsequent mask-evaporation of the Ni/ITO electrode pads and current injections. The morphologies and crystallization 50 nature of the ZnO NRs were characterized by field emission SEM (JEOL, JSM7600F, 10 kV) and XRD (Bruker, D2 PHASER, with Cu K$_a$ radiation). For room temperature PL measurements and PL mapping, the 266 nm line of a DPSS CW deep UV laser with a 10 µm diameter and a 20 mW power was used as the excitation 55 source. The PL measurement was performed through the front-side of the sample. The specular transmittance and reflectance spectra were measured, following which the absorption was obtained.

According to our design of LED devices, the size and 60 distributed density of Ag NPs affect the growth of the top layer (i.e., ZnO NRs) and the out-coupling of the LED's emission is mediated by LSP resonant modes; therefore, we fabricated Ag NPs with different dimensions to evaluate these effects. Thin films of Ag with different thicknesses of 5, 10 and 15 nm were 65 deposited on the top surface of the p-GaN layer by RF magnetron sputtering followed by the rapid thermal annealing (RTA) treatment to form nano-sized Ag NPs. Because of the self-organized nature after RTA treatment, the Ag NPs are randomly distributed and separated (meaning individual Ag NPs can be 70 treated independently), which is beneficial to capture light emitted in all direction inside LEDs because, for LSP excitation, there is no phase-matching condition as surface plasmon polariton.[20,33] Figures 1(a)–(c) indicate that the feature size of Ag NPs strongly depends on the pre-RTA deposited thickness of the 75 Ag films. The diameter of Ag NPs increases with the Ag film thickness, and the average diameters are estimated as 27 ±11, 58 ±25, and 109 ±43 nm for the pre-RTA deposited thicknesses of Ag films of 5, 10, and 15 nm, respectively. In contrast, the distributed density of Ag NPs exhibits the opposite tendency, 80 decreasing from 7.92×10^9 to 4.25×10^8 cm^{-2} with increasing pre-RTA deposited thickness of the Ag films [Fig. S2(a) in the ESI†]. There are three different Ag NP distributions, and we denote them as Ag NPs (5 nm), Ag NPs (10 nm), and Ag NPs (15 nm), referring to the 5, 10, and 15 nm annealed films, respectively. 85 The ZnO seed layer was directly sputtered onto the sample to cover the Ag NPs distributed on the p-GaN surface and was followed by hydrothermal treatment for the subsequent growth of ZnO NRs. The Ag NPs were embedded completely with the ZnO seed layer, which acts as a LSP resonance center for improving 90 the luminescence of n-ZnO NRs/p-GaN heterojunction LEDs. Figures 1(d)–(f) show the morphological evolution of ZnO NRs with three different Ag NPs embedded with a 30-nm-thick ZnO seed layer. The randomly aligned ZnO NRs of hexagonal (wurtzite) crystallography entirely covered the sample surface 95 despite the different dimensions of the Ag NPs distributed on the p-GaN surface. The diameters of the synthesized ZnO NRs depend largely on that of the Ag NPs embedded underneath and are irrelevant to the thickness of ZnO seed layer (Fig. S3 in the ESI†). The average size of the synthesized ZnO NRs is 100 approximately proportional to the dimensions of the Ag NPs, but the size exhibits a relatively weak variation from 60 to 80 nm with a distributed deviation of ±15 nm [Fig. S2(b) in the ESI†]. The average size is approximately 60 nm, 67 nm, and 80 nm for the ZnO NRs embedded with the Ag NPs (5 nm), Ag NPs (10 105 nm), and Ag NPs (15 nm), respectively. Additionally, the density of the synthesized ZnO NRs also decreased similarly to the Ag NPs, which decreased from 1.29×10^9 to 5.20×10^8 cm^{-2}, approximately one order of magnitude less than Ag NPs. The thickness of ZnO NRs [Figs. 1(g)–(i)], controllable by the 110 duration time of synthesis process, is approximately 292±6 nm, independent of the Ag NP dimensions embedded underneath. The thickness deviation is mainly attributed to the different growth rates of ZnO NRs along different crystallographic directions.[34,35]

115

Results and discussion

To obtain further insight into the LSP resonances of Ag NPs with different distributions, we plotted the normalized absorption spectra in Fig. 2(a), which were derived from the transmittance
5 and reflectance spectra. To clarify the influence of the LSP resonance of Ag NPs on the subsequently enhanced *PL/EL* spectra, we measured the absorption spectra of synthesized ZnO NRs with and without the Ag NPs (5 nm). The PL spectra of the bare ZnO NRs and p-GaN layer were measured and plotted in
10 Fig. 2(b) to determine whether the emission wavelengths match with the LSP resonance modes of Ag NPs. At first glance, a strong and a well-defined LSP absorption peak of λ=410 nm is observed for the Ag NPs (5 nm). However, the absorption profile becomes broader and weaker, accompanied by a clear red-shift in
15 the LSP absorption peak with increasing Ag NP diameter. The absorption intensity of Ag NP (15 nm) is still larger than that of Ag NP (10 nm) at the emission wavelength of λ=380 nm, which corresponds to the near-band-edge (NBE) transition of ZnO NRs. Therefore, it is reasonable to expect that Ag NPs (15 nm) have
20 better LSP-enhanced PL intensity of ZnO NRs than Ag NPs (10 nm). Such observation on the absorption spectrum agrees with previous reports suggesting that the distributed shape, dimensions, and density of Ag NPs affect the LSP resonance modes.[19,20,36] The ZnO NRs exhibit typical high absorption
25 behavior in the UV-light region, with a sharp cutoff-edge at the incident wavelength of λ=380 nm, which corresponds to the energy bandgap of ZnO NRs. For the ZnO NRs with Ag NPs (5 nm), a clear and broad absorption band with a peak wavelength of λ=433 nm can be observed, attributed to the strong LSP
30 resonance coupling of Ag NPs. Compared to the LSP absorption peak (λ=410 nm) of pure Ag NPs (5 nm), the red-shift of the absorption peak of Ag NPs is due to the different refractive index of the surrounding medium, which mediates the LSP resonance wavelength. [37] Nevertheless, the optical absorption of the
35 synthesized ZnO NRs with the Ag NPs (5 nm) at λ=380 nm still shows a high degree of overlap with the PL spectrum of ZnO NRs. For the PL results, the NBE transition of ZnO NRs is associated with the dominant peak at λ=380 nm, whereas the optical transition between the conduction band and deep defect
40 levels is attributed to the barely identified hump in the range of 450 nm ≤ λ ≤600 nm. High crystalline quality inherently exists in our synthesized ZnO NRs. Meanwhile, the p-GaN shows an emission peak near λ=440 nm, which is commonly observed and is attributed to a consequence of the transition from the
45 conduction band or shallow donor to the Mg acceptor levels. Accordingly, we can reasonably expect that Ag NPs (5 nm) will give the largest LSP enhancement on the UV emission of ZnO NRs because their LSP resonance peak shows the highest degree of overlap with the PL spectrum of ZnO NRs compared to the
50 other two Ag NP distributions. In this study, we also change the thickness of the ZnO seed layer and will later discuss its influence on the out-coupling of excited LSP resonances. First, we have to examine the optical properties of these ZnO seed layers. Figure 2(c) shows the PL spectra of ZnO seed layers
55 grown on a sapphire substrate with thicknesses of (i) 10, (ii) 30, and (iii) 50 nm. The PL spectrum of (iv) 30-nm-thick ZnO seed layer grown on p-GaN layer with Ag NPs (5 nm) is also plotted in the figure. Due to the nature of the amorphous phase in the

ZnO seed layer, the UV emission related to the NBE
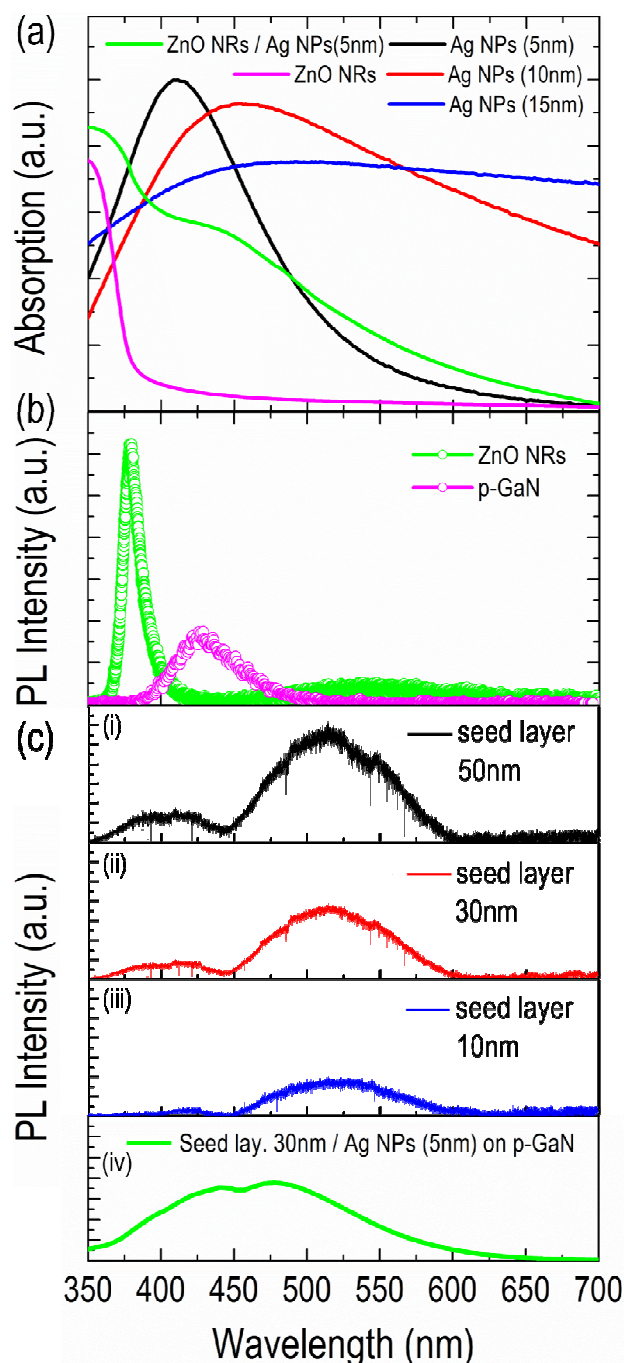
Fig. 2. Absorption spectra of Ag NPs with various distributions and that of the synthesized ZnO NRs with and without Ag NPs (5 nm). (b) PL spectra of bare ZnO NRs and the p-GaN layer. (c) PL spectra of ZnO seed layers with different thicknesses of (i) 10, (ii) 30, and
65 (iii) 50 nm, respectively. (iv) PL spectrum of a 30-nm-thick ZnO seed layer grown on a p-GaN layer with Ag NPs (5 nm).

transition was observed on all of these ZnO seed layers but was relatively weak and broad, and the radiative recombination
70 associated with the deep level emissions in the visible-light region became more pronounced with increasing ZnO seed layer thickness. The *PL* spectrum of the ZnO seed layer/Ag NPs (5 nm)

prepared on p-GaN layer is similar to that of the bare ZnO seed layer grown on the sapphire substrate, except that there is an additional emission peak approximately 440 nm corresponding to the energy transition of Mg related acceptors in the p-GaN layer.
5 Therefore, the amorphous nature (or defect state density) of the ZnO seed layer is unaffected, despite using the different substrates (sapphire or p-GaN) to grow the ZnO seed layer. The measured *PL* spectra shown in Fig. 2 confirm that the UV emission by NBE transition is attributed to the radiative emission
10 of ZnO NRs, which is irrelevant to the ZnO seed layer underneath and is valid in terms of the consideration of the *EL* spectra, as will be discussed later in the article. Figure S4(a) in the ESI† shows the X-ray diffraction (XRD) patterns of ZnO NRs with (blue line) and without (black line) Ag NPs (5 nm). The XRD
15 pattern of bare Ag NPs (5 nm) distributed on the sapphire substrate is also plotted in the figure for comparison. The diffraction peaks of both ZnO NRs samples are well-defined and display the typical hexagonal wurtzite structure with orientations at 2θ=31.76°, 34.41°, 36.24°, 47.52°, 56.58°, and 62.84°, which
20 correspond to the (100), (002), (101), (102), (110), and (103) planes, respectively. Among them, (002) is the most preferred orientation of growth. These diffraction peaks can be indexed and correspond to the XRD pattern of the referential ZnO (JCPDS card no. 36-11451), referring to the bottom of Fig. S4(a). A
25 diffraction peak at 2θ=38.10°, attributed to the (111) plane of the face-centered cubic structure of metallic silver, is clearly observed on the bare Ag NPs, but a similar diffraction peak from the (111) plane is hardly observed on ZnO NRs with Ag NPs because ZnO NRs interfere with the receiving of the diffracted X-
30 ray signals of Ag NPs. The standard deviation (SD) of the XRD intensity for samples with and without Ag NPs was estimated using the govern relation:[38]

$$SD = \sqrt{\frac{\sum_{i=1}^{N} I(hkl)_i^2 - \frac{\left(\sum_{i=1}^{N} I(hkl)_i\right)^2}{N}}{N}}$$

(1)

35 where $I(hkl)_i$ stands for the measured peak intensity of the $(hkl)_i$ plane, and N is the number of diffraction peaks observed in the XRD pattern. The SD values of ZnO NRs with and without Ag NPs are SD=0.32 and SD=0.34, respectively, and this slight difference indicates that ZnO NRs samples exhibit very similar
40 crystalline qualities and that the prior formation of Ag NPs distributed on the p-GaN surface does not adversely affect the synthetic quality of the subsequent ZnO NRs. We also verified the preferred orientation of the synthesized ZnO NRs by evaluating the texture coefficient (*TC*) value given by:[39]
45

$$TC(hkl)_i = \frac{\dfrac{I(hkl)_i}{I_0(hkl)_i}}{\dfrac{1}{N}\displaystyle\sum_{i=1}^{N}\dfrac{I(hkl)_i}{I_0(hkl)_i}}$$

(2)

where $I_0(hkl)_i$ is the standard intensity (JCPDS) of the $(hkl)_i$ plane. As expressed in Eq. (2), a deviation of *TC* value farther from unity corresponds to the higher preferred orientation of the *(hkl)*

50 plane in the ZnO NRs. The distributed profiles of the derived texture coefficient (*TC*) values against the diffracted crystalline planes $[(hkl)_i]$ present similar tendency for both samples of interest [Fig. S4(b) in the ESI†]. The characteristic diffraction peak associated with the (002) plane is strongly textured, which
55 indicates that both samples prefer to grow along the c-axis direction, regardless of the incorporation of Ag NPs, agreeing well with the SEM observation shown in Fig. 1.
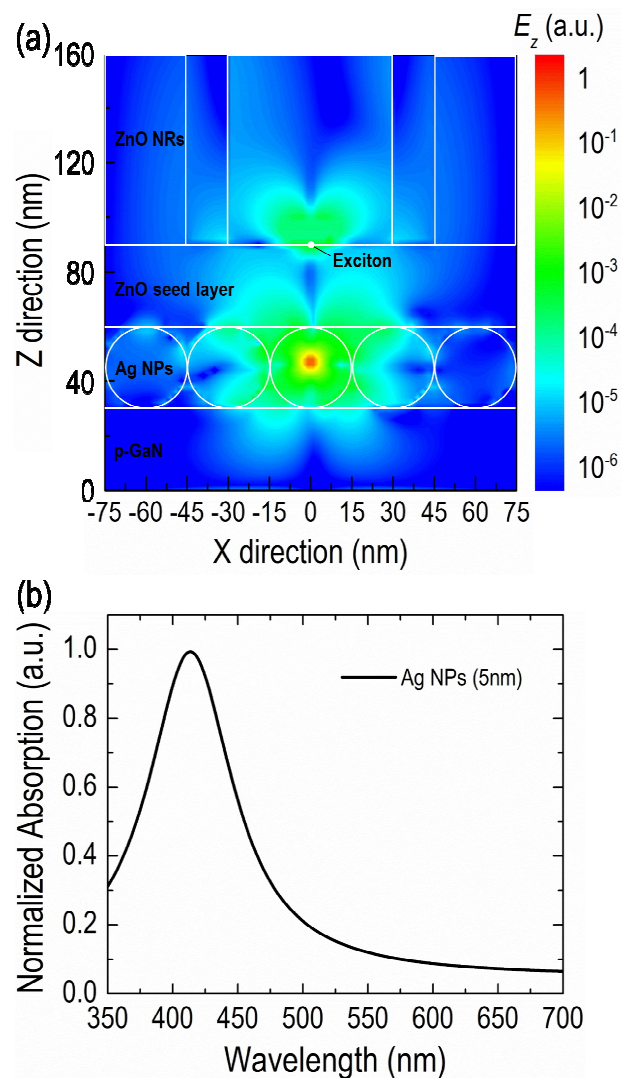

60 **Fig. 3.** (a) Electric field distribution of LSP mode after exciting by a dipole source (λ=380 nm) oscillating in the center of the Ag NP (5nm). (b) Calculated absorption spectrum of Ag NPs (5nm).

Figure 3(a) plots the electric field distribution of Ag NPs for
65 a set of parameters described as follows: Ag NPs (5 nm) of 30 nm in diameter and a 30-nm-thick ZnO seed layer (n=2.25), infinitely thick p-GaN layer (n=2.62) and a dipole source (λ=380 nm) oscillating in the center of the Ag NP to excite the LSP mode. An exciton radiation source with emission wavelength of 380 nm is
70 also introduced in the bottom of the ZnO NRs to discuss the possible optical interactions (near-field or far-field optical couplings) between the LSP mode of Ag NPs and the exciton of

ZnO NRs. Figure 3(b) displays the absorption spectrum for the Ag NPs of these dimensions. Accordingly, the electric field of Ag NPs is strongly confined near the surfaces of the NPs, and the field intensity varies as $\exp(-r/\delta)$ along the radial direction (r) of the NPs. δ is estimated to be 9 nm, which is smaller than the separation distance (the thickness of the ZnO seed layer) between the ZnO NRs and the Ag NPs of our samples in this study. Therefore, the near-field optical coupling between the excitons of the ZnO NRs and the LSP of Ag NPs is relatively weak, but the far-field optical coupling via the photon-LSP resonance interaction is dominant. The absorption spectrum due to the LSP resonance exhibits a strong and a well-defined LSP absorption peak of λ=410 nm [Fig. 3(b)], which qualitatively follows the experimental results, confirming the reliability of the numerical simulations of *FDTD*. Additionally, the theoretical modeling indicates that our hybridized nanostructure has great potential for LSP-enhanced far-field coupling in ZnO NRs/p-GaN LEDs.

Next, we discuss the influence of the surface morphology of the ZnO seed layer on the out-coupling of the excited LSP resonances. Figure 4(a) shows the normalized PL spectra of ZnO NRs synthesized on a sapphire substrate with and without Ag NPs (5 nm). The PL mapping at the peak intensity of λ=380 nm for ZnO NRs with (left) and without (right) Ag NPs (5 nm) over a square range of 900 μm×900 μm is also inserted in the figure. The PL spectrum of ZnO NRs with Ag NPs (5 nm) (i.e., the smallest dimension of the Ag NP distribution) is normalized to the peak value of bare ZnO NRs. The PL spectra of the ZnO NRs with Ag NPs (10 nm) and Ag NPs (15 nm) were also measured, but they are not shown in the figure for clarity. The PL intensity of ZnO NRs with Ag NPs (5 nm) is substantially higher than that of bare ZnO NRs. We observe a factor of ~2.4 enhancement of the PL peak intensity of the UV emission centered at λ=380 nm, whereas the deep level emission centered at λ=550 nm exhibits slightly enhanced PL spectrum. The PL mapping profile shows a sharp boundary between the regions with and without Ag NPs (5 nm), and a uniform and consistent boost of the PL intensity is clearly observed over the entire treatment ZnO NRs. Figure 4(b) shows the enhanced factor of the PL peak intensity (at λ=380 mm) against the variation of the Ag NP distribution and against the average diameter of the ZnO NRs (in the secondary horizontal-axis) for three different thicknesses of ZnO seed layers (10, 30, and 50 nm). At a given thickness of ZnO seed layer, the enhanced factor of the PL peak intensity is determined by the overlapping degree between the LSP resonance peak and the PL spectrum of the ZnO NRs (Fig. 2), which is mainly associated with the diameters of the Ag NPs and is irrelevant to the distributed diameters of the synthesized ZnO NRs. The contribution of the nano-size effect on the enhanced *PL* emission is insignificant, probably because of the relatively small invariance of the diameters in the synthesized ZnO NRs. Most importantly, the ZnO NRs with Ag NPs (5 nm) exhibit the largest enhanced PL intensity ranging from ~1.9 to ~2.4, which is mainly determined by the thickness of the ZnO seed layer that surrounds the Ag NPs. This result agrees well with our previous discussion of Fig. 2(a) because the PL emission of ZnO NRs shows the highest degree of overlap with the LSP absorption peak of Ag NPs (5 nm).

Likewise, the absorption profile of Ag NPs (10nm) deviates more from the PL spectrum of ZnO NRs and thus corresponds
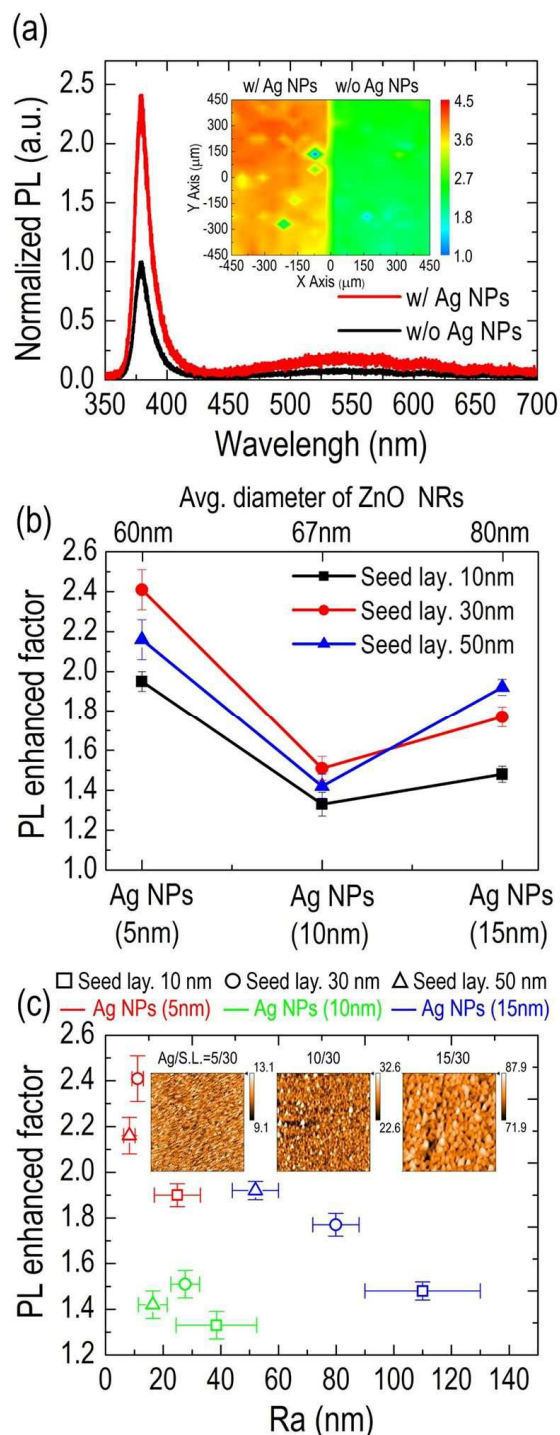

Fig. 4. (a) Normalized PL spectra of ZnO NRs synthesized on the sapphire substrate with and without Ag NPs (5 nm). Inset shows the corresponding PL mapping profile. (b) Enhanced factor of the PL peak intensity (at λ=380 mm) against the variation of the Ag NP distributions and against the average diameter of ZnO NRs (in the secondary horizontal-axis) for three different ZnO seed layer thicknesses (10, 30, and 50 nm). (c) Enhanced factor of the PL peak intensity (at λ=380 mm) versus the arithmetic average (Ra) of the surface roughness for various Ag NP distributions covering different ZnO seed layer thicknesses (10, 30, and 50 nm).

to the smallest enhanced factor of approximately 1.3−1.5. When considering the effect of surface morphology, a 30-nm-thick ZnO seed layer generally shows the highest enhanced PL intensity under a given Ag NP distribution, indicating that the surface morphology of the surrounding medium of Ag NPs is also important for the interaction with excited LSP resonances. To discuss in more detail the dependence of the enhanced PL intensity on the surface morphology of the surrounding medium of LSP resonant centers, Fig. 4 (c) plots the enhanced PL intensity of ZnO NRs (at λ=380 nm) against the arithmetic average (Ra) of the surface roughness for various Ag NP distributions (5, 10, and 15 nm) covering different ZnO seed layer thicknesses (10, 30, and 50 nm). The Ag NPs (5 nm), which correspond to the smallest dimension, are direct and easy for the sputtering gas-flow to fill in completely, so they have the smoothest surface and lowest Ra value, as plotted in the inset of Fig. 4(c). The sample of Ag 15 nm NPs shows the reverse tendency and has the largest Ra value. The Ra values measured by atomic force microscopy (AFM) for Ag NPs (5 nm), Ag NPs (10 nm), and Ag NPs (15 nm) covering a 30 nm ZnO seed layer

are 11.1, 27.6, and 79.9 nm, respectively. However, compared to the surface morphology of the ZnO seed layer, the Ag NPs dimensions play a more important role in terms of the enhanced PL intensity. Nevertheless, this work provides general guidelines for designing a high UV emission nanostructured LED based on the ZnO NRs configuration by tuning the LSP coupling effect by varying the Ag NPs distributions, which can be further modified in a controlled manner by varying the surface morphology of the surrounding medium of Ag NPs.

The PL spectrum and AFM morphology analysis reveal that the ZnO NRs with Ag NPs (5 nm) covered by a 30 nm ZnO seed layer exhibit the highest enhanced factor of the PL spectrum, which prompted us to use these conditions for device fabrication. Figure 5(a) shows a schematic of our n-ZnO NRs/p-GaN heterojunction LED with randomly distributed Ag NPs. The slanted indium-tin-oxide (ITO) film deposited on top is used to directly bridge and interconnect each ZnO NR for efficient current injections and also serves as a platform
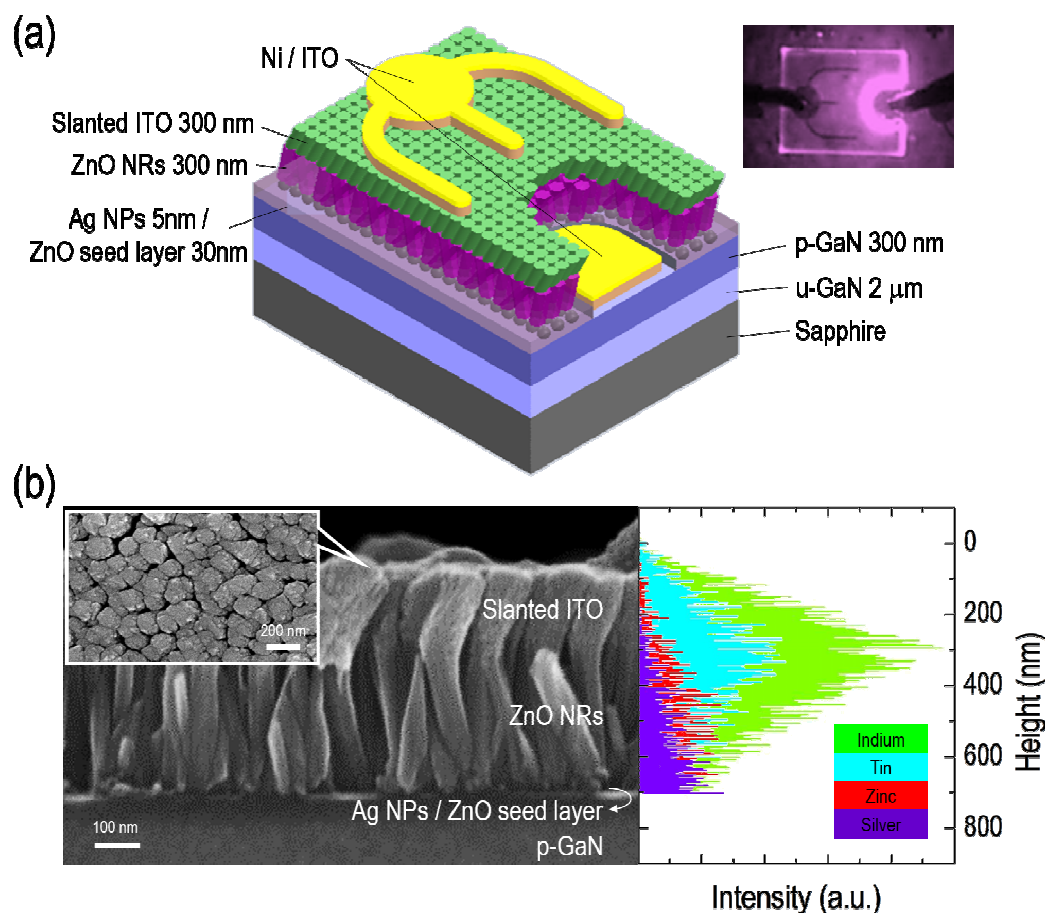

Fig. 5. (a) Design architecture of the n-ZnO NRs/p-GaN heterojunction hybridized Ag NPs. Inset: photograph of the fabricated LED device with a chip size of 300 μm×300 μm under an injection current of 100 mA. (b) Cross-sectional SEM images of the fabricated LED device. Inset: an enlarged top-view SEM image of the surface of the slanted ITO film. Right-hand side image: a cross-sectional elemental profile of the fabricated structure determined by energy dispersive X-ray spectroscopy (EDX) and measured along the direction traversing the interface between the ZnO NRs and p-GaN layer.

for the subsequent fabrication of electrical pads. The photograph of a fabricated LED device with a chip size of 300 μm×300 μm under an injection current of 100 mA is shown in the inset of Fig.

5(a), which emits violet light that can be directly identified by the naked eye. The SEM images in Fig. 5(b) present the results of ZnO NRs with Ag NPs (5 nm) on the top of the p-GaN layer, and

as expected, the slanted ITO film successfully interconnects the ZnO NRs. According to the top-view SEM image of the same LED device shown in the inset, the surface morphology of the slanted ITO film is nearly continuous but is still porous. Energy dispersive X-ray spectroscopy (EDX) was also applied to analyze and confirm the cross-sectional compositional profile of the fabricated device, measured from the top surface of the slanted ITO film to the Ag NPs, as plotted in the right-hand side of Fig. 5(b). The signals of indium and tin elements were able to be traced, even down to the region where ZnO NRs is located, meaning that a partial of the periphery/sidewall of ZnO NRs is covered by ITO, although we used the oblique-angle sputtering method to deposit the slanted architecture. Such phenomenon could be attributed to the energy transfer through multiple collision processes, by which indium and tin atoms gain sufficient kinetic energy to migrate along the axial directions of the ZnO NRs, creating undesirable leakage paths where injected currents bypass the path along the n-ZnO NRs/p-GaN heterojunctions. The influence of the migration of compositional elements along the ZnO NRs on the electrical characteristics of the fabricated devices will be discussed later in more detail. The EDX spectrum also indicates that Ag element is present and extends into the ZnO NR region, suggesting that a similar migration behavior of silver atom is likely to occur during the fabrication, which again, will result in an unintended short-circuit path for electrical currents. However, we detect the highest signal intensity of silver element near the junction region of n-ZnO NRs/p-GaN, indicating the location where most of the Ag NPs accumulate.

To characterize the electrical properties of our proposed n-ZnO NRs/p-GaN heterojunction LEDs hybridized with Ag NPs (5 nm), the current versus voltage (*I-V*) characteristics were measured in the dark at room temperature. Figure 6(a) shows the measured *I-V* curves of LEDs with and without Ag NPs (5 nm) in linear scales, which were re-plotted again in a semilogarithmic scale in the inset to examine the leakage current behavior. Both LEDs have very similar turn-on voltages, which are 4.51 V and 5.02 V for the proposed LED structure hybridized with Ag NPs (5 nm) and its counterpart, respectively, similar to the typical values of n-ZnO/p-GaN heterojunction LEDs published in the literature.[1,2] The fabricated LED devices have good ohmic-contact in both the anode and cathode metals. In addition, leakage currents on the order of 9.75×10^{-5} A and 1.41×10^{-4} A at -10 V are measured for the n-ZnO NRs/p-GaN LEDs with and without Ag NPs (5 nm), respectively, which corresponds to generally acceptable values for shunt resistances of R_P= 1.75 MΩ and R_P= 1.70 MΩ. These results indicate that the partial migration of slanted ITO film and Ag NPs toward the ZnO NRs region does not cause significant deterioration of the electrical characteristics of the LED devices. Figure 6(b) plots $I(dV/dI)$ versus I to determine the series resistance (R_s) and the ideality factor (n_{ideal}) for both LED devices according to the differential form of the Shockley equation described by $I(dV/dI) = R_s \times I + \text{n}_{ideal} \times (kT/e)$,[40] where k and T denote the Boltzmann constant and ambient temperature, respectively. The extracted values of R_s and n_{ideal} are R_s=577.98 Ω, and R_s=864.87 Ω, and n_{ideal}=15.14 and n_{ideal}=14.48 for n-ZnO NRs/p-GaN heterojunction LEDs with and without Ag NPs (5 nm), respectively. Unlike the traditional LEDs designed as a planar layer and the bulk configuration, the proposed LED

structure is composed of numerous nano-sized LEDs (~10^9 cm^{-2}) that are effectively connected in parallel and are accompanied by anomalously high values of R_s and n_{ideal}.[14] Additionally, the tunneling effect, enhanced by the nanoscale features of ZnO NRs, induces the transport of injected carriers through the junction region of the LED, which may also lead to an unusually and extremely large ideality factor.[41] Most importantly, the electrical characteristics of the LED device with Ag NPs (5 nm) are comparable or even better than those of its counterpart reference, which again indicates that the introduction of Ag NPs does not cause adverse effects on the n-ZnO NRs/P-GaN heterojunction LEDs.
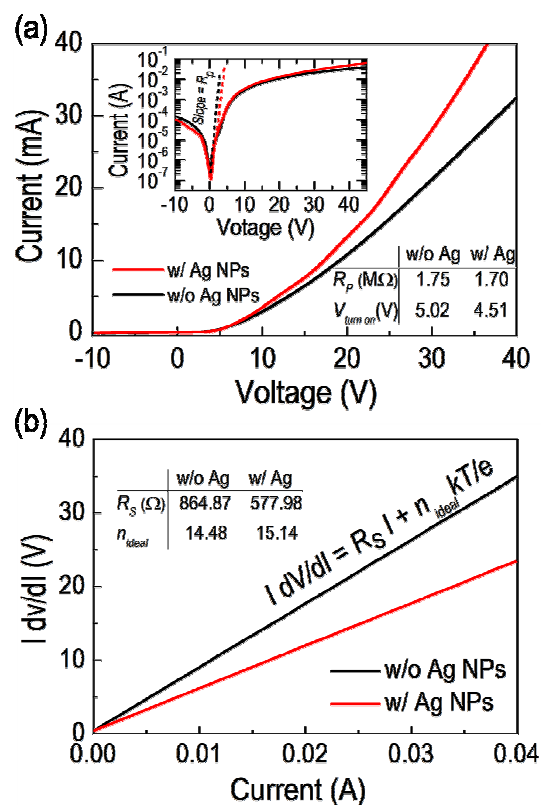

Fig. 6. (a) Current vs. voltage (*I-V*) behavior of n-ZnO NRs/p-GaN heterojunction LEDs with and without Ag NPs (5 nm). Inset: The same *I-V* current plotted on a semi-log scale. The turn-on voltage ($V_{turn-on}$) and shunt (R_P) resistance extracted from the *I-V* curve are also summarized in the figure. (b) $I(dV/dI)$ versus I curves to extract the series resistance (R_s) and ideality factors (n_{ideal}) of both LEDs. The extracted values of R_s and n_{ideal} are also summarized and inserted in the figure.

Figure 7(a) shows light-output power versus forward injection current (*L-I* curve) of n-ZnO NRs/p-GaN heterojunction LEDs with and without Ag NPs (5 nm). Only the light-output powers of UV emission (hv_{ZnO}) were captured for both LEDs and were then plotted as the *L-I* curves shown in Fig. 7(a). Accordingly, the light-output power of the hv_{ZnO} emission of n-ZnO NRs/p-GaN heterojunction LEDs with Ag NPs (5 nm) is considerably higher than that of the reference LED without Ag NPs (5 nm). The light-output power of hv_{ZnO} emission increases gradually with a mild and steady slope when we increase the forward current injected into the reference LED. In contrast, on the treatment LED with

Ag NPs (5 nm), we observe a sublinear dependence on the *L-I* curve (*I* ≤60 mA), which retains a steeper slope than the reference LED and becomes superlinear when further increasing the injected current (*I*>60 mA). As a result, the enhanced ratio of the light-output power of $h\nu_{ZnO}$ emissions between the treatment and reference LEDs exhibits a clear boost from ~1.5 to ~2.0 at the high injected current of *I*>60 mA, as illustrated in the inset of Fig. 7(a). This EL enhanced factor (~1.5−~2.0) generally agrees with the measured PL enhanced value (~ 2) for Ag NPs (5 nm), as shown in Fig. 4(b). Hence, we can attribute most of the EL enhancement to the LSPs resonant coupling effect. Because the LSPs resonant coupling effect should not depend on the injection current, the observed phenomenon of boosting the enhancing factor from ~1.5 to ~2.0 at high injection current suggests an additional mechanism in the treatment LED with Ag NPs (5 nm). To understand this additional mechanism, Figure 7(b) shows the EL spectra of n-ZnO NRs/p-GaN heterojunction LEDs with Ag NPs (5 nm) for various injected currents, ranging from *I*=20 mA

to *I*=100 mA with a current interval of 10 mA. For *I* ≤60mA, three distinctive EL peaks related to the energy transitions of NBE in ZnO NRs ($h\nu_{ZnO}$), the Mg acceptor levels in p-GaN ($h\nu_{GaN}$), and deep defect levels in ZnO NRs ($h\nu_{defect}$), respectively, can be distinguished. Compared to the *PL* emission of ZnO NRs [Fig. 4(a)], the $h\nu_{defect}$ luminescence associated with the radiative recombination of excess carriers from the interface (defect) states of n-ZnO NRs/p-GaN heterojunctions is more significant and can be clearly observed on the *EL* emission of our LED devices because the *PL* emission is the recombination of excess carriers near the surface region of ZnO NRs (depending on the optical intensity of the excitation light source), whereas *EL* emission has to take into account the interface (defect) recombination because the excess carriers are produced by injecting current into the n-ZnO NRs/p-GaN heterojunction. Furthermore, due to the nano-sized geometry of the n-ZnO NRs, the density of states (DOS) and the radiative recombination rate of injected carriers could be quantized   and   enhanced   when
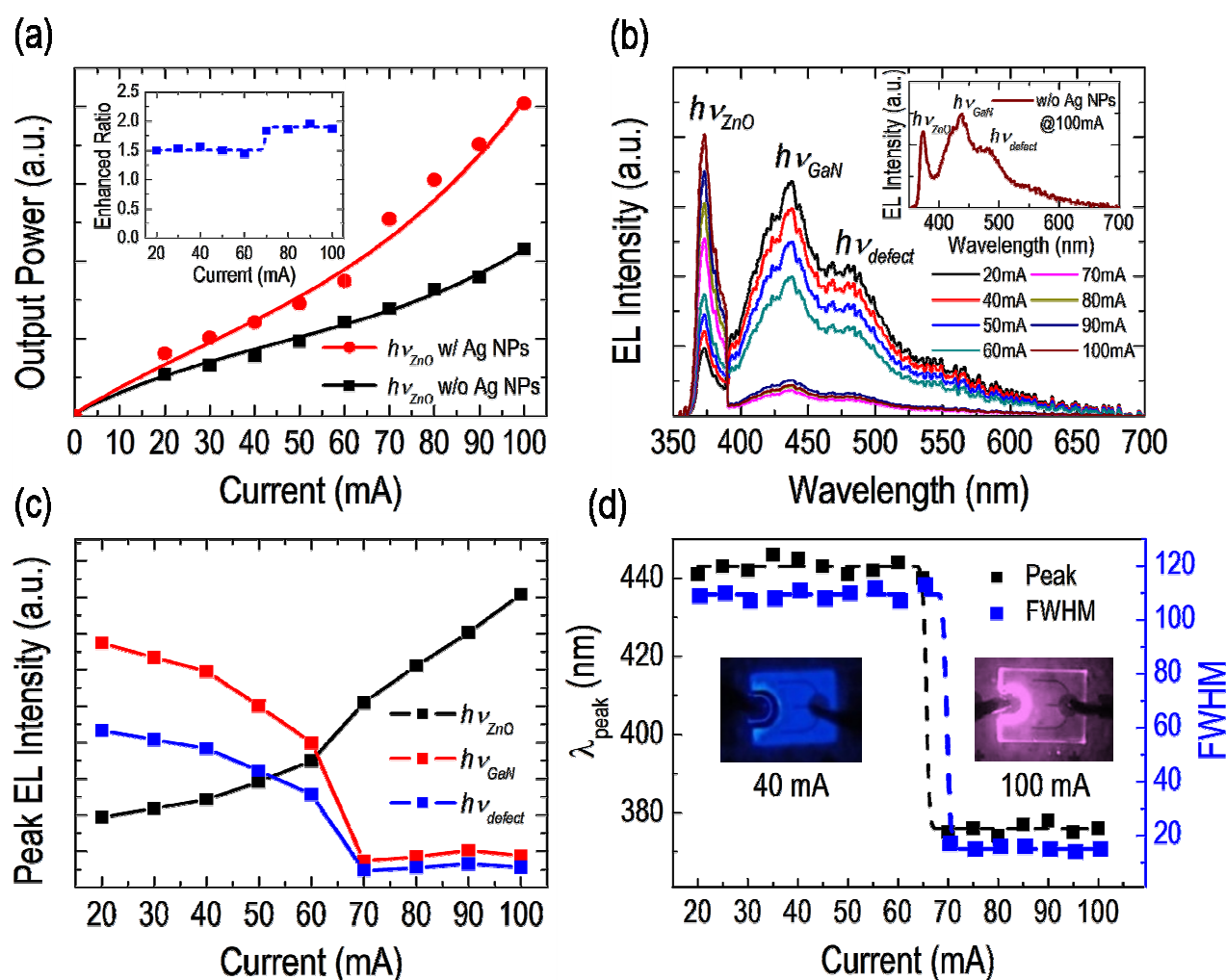

Fig. 7. (a) Light-output power vs. injection current for n-ZnO NRs/p-GaN heterojunction LEDs with and without Ag NPs (5 nm). Inset: enhanced ratio of the light-output power between the treatment and reference LEDs versus the injected current. (b) EL spectra of the n-ZnO NRs/p-GaN heterojunction LED with Ag NPs (5 nm) under various injection currents. Inset: EL spectrum of the reference LED under *I*=100 mA. (c) EL peak intensity vs. injected current for $h\nu_{ZnO}$, $h\nu_{GaN}$ and $h\nu_{defect}$ emissions of n-ZnO NRs/p-GaN heterojunction LEDs with Ag NPs (5 nm). (d) The position and FWHM of the dominant peak versus injection current. Photographs of n-ZnO NRs/p-GaN heterojunction LEDs with Ag NPs (5 nm) under 40 mA and 100 mA are also shown in the inset of (d).

considering the quantum confinement effect. Consequently, most of the injected electrons were confined within the ZnO NRs and eventually recombined radiatively to emit ultraviolet light,
[5] although the electron concentration and mobility of the ZnO NRs are both larger than those of the p-GaN layer. However, further studies are necessary to understand and confirm the recombination details of the injected carriers for such hybridized-nanostructure LEDs. The EL intensity of hv_{ZnO} emission becomes
[10] stronger as the injected current increases, whereas that of hv_{GaN} and hv_{defect} emissions behaves in the opposite way, decreasing with increasing injected current. With an injected current I >60 mA, the EL spectrum shows only one dominant peak of hv_{ZnO} emission, and the hv_{GaN} and hv_{defect} emissions become hard to
[15] identify, suggesting the NBE transition of ZnO NRs predominates the EL spectrum in this stage. As shown in the inset of Fig. 7(b), although the same three distinguishable EL peaks corresponding to hv_{ZnO}, hv_{GaN} and hv_{defect} emissions are retained in the reference LED without Ag NPs, those EL peaks can still be
[20] identified even under the high injected current of I=100 mA. The intensities of these EL peaks simultaneously increase with increasing injected current (not shown here), which again illustrates a fundamental difference of the radiative recombination mechanisms between n-ZnO NRs/p-GaN heterojunction LEDs
[25] with and without Ag NPs. Figure 7(c) shows the EL peak intensity as a function of the injected current for all hv_{ZnO}, hv_{GaN} and hv_{defect} emissions of n-ZnO NRs/p-GaN heterojunction LEDs with Ag NPs (5 nm). hv_{ZnO} emission gradually increases at I ≤60 mA and shows a sharp rise after that level. hv_{GaN} and hv_{defect}
[30] emissions exhibit an opposite tendency, gradually decreasing (but still higher than hv_{ZnO} emission) at I ≤60 mA and then falling off significantly to an extremely low intensity. Therefore, the position and FWHM for the dominant peak of the corresponding EL spectrum change from hv_{GaN} to hv_{ZnO} emissions at high
[35] injected current (Fig. 7(d)) and is accompanied by a nearly 2-fold enhancement in the light-output power of hv_{ZnO} emission compared to that of the reference LEDs without Ag NPs (5 nm). The change of emission wavelengths can also be identified qualitatively by the naked eye, as shown in the photographs of the
[40] device at injection currents of 40 mA and 100 mA (inset of Fig. 7(d)). According to the EL spectra of the treatment and reference LEDs at the same injection current larger than 60 mA, nearly all of the injected carriers for the treatment LEDs contribute to the UV emission, but only some of the injected carriers for the
[45] reference LED contribute to the UV emission (and the rest of the injected carriers contribute to visible emission). However, for same injection current of less than 60 mA, only some of the

injected carriers for both LEDs contribute to UV emission. The change of the ratio of the injected carrier contribution to UV
[50] emissions at high injection current could explain the increase of the enhanced factor from ~1.5 to ~2.0.

A possible reason for such a change in the EL spectrum can be explained as follows. For the treatment device, the Ag NPs are located at the interface between the ZnO NRs and p-GaN layer.
[55] The corresponding energy band diagram of such a device at zero bias is plotted in Fig. 8 (a), according to the working function of Ag,[42] the electron affinity of ZnO and GaN,[43,44] and the Fermi level of n-ZnO and p-GaN. Based on the theory of metal-semiconductor junctions, the n-ZnO/Ag junction forms an Ohmic
[60] contact, and the Ag/p-GaN becomes a Schottky contact. Due to the large difference between the work functions of Ag and p-GaN, the Schottky barrier is bent downward strongly so that electrons can tunnel through the barrier and possibly form an inversion layer at the interface. Under a small forward bias (or low
[65] injection current), the minority carrier of electrons at the Ag/p-GaN interface can jump to the Mg acceptance level and emit photons of hv_{GaN}, and the holes from p-GaN can enter the n-ZnO NRs to recombine with electrons and emit photons of hv_{defect} and hv_{ZnO}, as shown in Fig. 8 (b). However, as increasing the forward
[70] bias (still under regime of low injection current) leading to the lowering of the Schottky barrier, the electrons existing at the Ag/p-GaN interface become relatively less and electrons from n-ZnO become more difficult to tunnel through the barrier so that might occupy the defect level of ZnO, leading to the decrease of
[75] EL intensity of hv_{GaN} and hv_{defect} as injection current increases. At larger forward bias (or high injection current as shown in Fig. 8(c)), the electrons of inversion layer at the Ag/p-GaN interface disappear; therefore, electrons occupy and saturate most of the defect level of ZnO, leading to the EL intensity of hv_{GaN} and
[80] hv_{defect} becoming very weak. For reference LEDs without the Ag NPs at the interface between n-ZnO NRs and p-GaN, the energy band diagram is not modified by the Ag NPs, as shown in Fig. 8(d) (for zero bias). For this band diagram, regardless of the size of the applied forward bias, electrons can always jump to the Mg
[85] acceptor level and the defect level of ZnO to emit photons of hv_{GaN} and hv_{defect}. More investigations are needed to understand the real physical mechanism causing the different behaviors of the EL spectra of the treatment and reference devices. Nevertheless, our results show that introducing Ag NPs between
[90] n-ZnO NRs and p-GaN can pave the way for better structure design of efficient UV-emission LEDs.
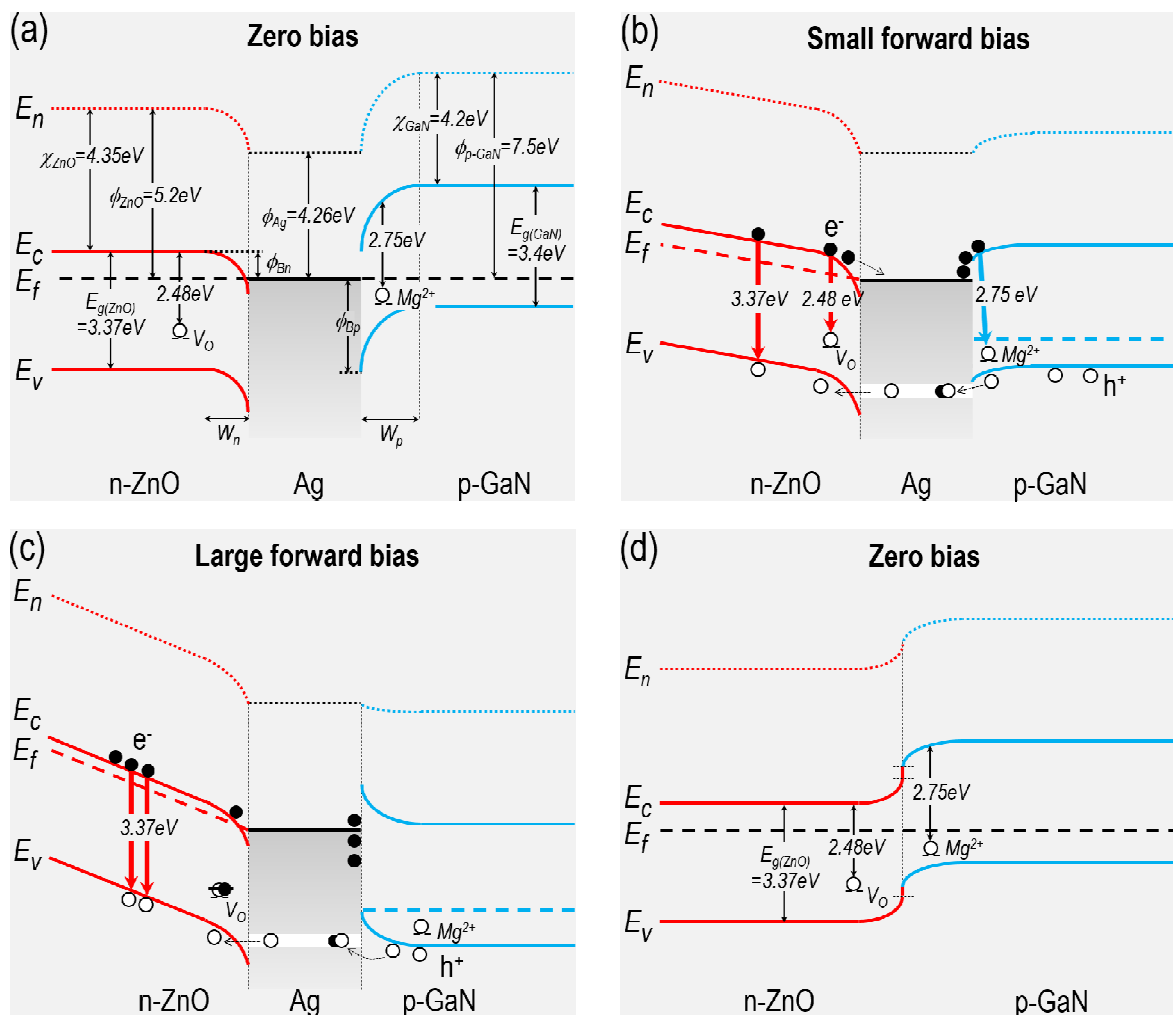
Fig. 8. The energy band diagram of n-ZnO NRs/p-GaN heterojunction LEDs with Ag NPs under (a) zero bias, (b) small forward bias, and (c) large forward bias. (d) The energy band diagram of n-ZnO NRs/p-GaN heterojunction LEDs without introducing Ag NPs under zero bias.

Conclusions

In summary, we fabricated Ag NPs-incorporated n-ZnO NRs/p-GaN heterojunctions by facilely hydrothermally growing ZnO NRs on Ag NPs-covered GaN. The performance of the hybridized-nanostructure LEDs was systematically examined and was found to be better than that of LEDs without incorporated Ag NPs. By comparing the devices with and without Ag NPs, we provide a detailed mechanism of how Ag NPs enhance UV emission through LSPs resonant coupling effect and facilitate carrier injection by the modification of the electronic band structure at the interface between n-ZnO NRs and p-GaN. As a result, this work paves the way for developing advanced nanostructured LED devices with high luminescence efficiency in the UV-emission regime.

Notes and references

[a] Institute of Electro-Optical Science and Technology, National Taiwan Normal University, 88, Sec.4, Ting-Chou Road, Taipei 116, Taiwan Fax: +886-2-86631954; Tel: +886-2-77346733;E-mail: yajulee@ntnu.edu.tw
[b] Institute of Photonic System, National Chiao-Tung University, 301, Gaofa 3rd Road, Tainan 711, Taiwan; E-mail: zupoyang@nctu.edu.tw

c *Solid-State Lighting Systems Department, Green Energy and Environment Research Laboratories, Industrial Technology Research Institute (ITRI), Hsinchu 310, Taiwan*

d *Department of Photonics, National Cheng Kung University, 1, University Rd., Tainan, 701, Taiwan*

e *Department of Electrical Engineering, Chang Gung University, 259, Wen-Hwa 1st Rd., Kwei-Shan Dist., Taoyuan, 33302, Taiwan*

1   G. C. Park, S. M. Hwang, S. M. Lee, J. H. Choi, K. M. Song, H. Y. Kim, H.-S. Kim, S.-J. Eum, S.-B. Jung, J. H. Lim and J. Joo, *Sci. Rep.*, 2015, **5**, 10410.

2   Z. P. Yang, Z. H. Xie, C. C.Lin, and Y. J. Lee, *Opt. Mater. Express*, 2015, **5**, 399.

3   Y.-Q. Bie, Z.-M. Liao, P.-W. Wang, Y.-B. Zhou, X.-B. Han, Y. Ye, Q. Zhao, X.-S. Wu, L. Dai, J. Xu, L.-W. Sang, J.-J. Deng, K. Laurent, Y. Leprince-Wang and D.-P. Yu, *Adv. Mater.*, 2010, **22**, 4284.

4   C.-H. Chen, S.-J. Chang, S.-P. Chang, M.-J. Li, I-Ch. Chen, T.-J. Hsueh and C.-L. Hsu, *Appl. Phys. Lett.*, 2009, **95**, 223101.

5   M.-C. Jeong, B.-Y. Oh, M.-H. Ham, S.-W. Lee and J.-M. Myoung, *Small*, 2007, **3**, 568.

6   E. Lai, W. Kim and P. Yang, *Nano Res.*, 2008, **1**, 123.

7   L. Zhang, Q. Li, L. Shang, F. Wang, C. Qu and F. Zhao, *Opt. Express*, 2013, **21**, 16578.

8   Z.-P. Yang, Z.-H. Xie, C.-C. Lin and Y.-J. Lee, *Opt. Mater. Express*, 2015, **5**, 399.

9   Q. Li, V. Kumar, Y. Li, H. Zhang, T. J. Marks and R. P. H. Chang, *Chem. Mater.*, 2005, **17**, 1001.

10 G. Hua, Y. Zhang, C. Ye, M. Wang and L. Zhang, *Nanotechnology*, 2007, **18**, 145605.

11 K.-K. Kim, S.-d. Lee, H. Kim, J.-C. Park, S.-N. Lee, Y. Park, S.-J. Park and S.-W. Kim, *Appl. Phys. Lett.*, 2009, **94**, 071118.

12 J. Zhong, H. Chen, G. Saraf, Y. Lu, C. K. Choi, J. J. Song, D. M. Mackie and H. Shen, *Appl. Phys. Lett.*, 2007, **90**, 203515.

13 J. Zhong, S. Muthukumar, Y. Chen, Y. Lu, H. M. Ng, W. Jiang and E. L. Garfunkel, *Appl. Phys. Lett.*, 2003, **83**, 3401.

14 Y.-J. Lee, Z.-P. Yang, F.-Y. Lo, J.-J. Siao, Z.-H. Xie, Y.-L. Chuang, T.-Y. Lin and J.-K. Sheu, *APL Mater.*, 2014, **2**, 056101.

15 H. Jeong, D. J. Park, H. S. Lee, Y. H. Ko, J. S. Yu, S.-B. Choi, D.-S. Lee, E.-K. Suh and M. S. Jeong, *Nanoscale*, 2014, **6**, 4371.

16 B.-U. Ye, B. J. Kim, Y. H. Song, J. H. Son, H. k. Yu, M. H. Kim, J.-L. Lee and J. M. Baik, *Adv. Funct. Mater.*, 2012, **22**, 632.

17 K. Okamoto, I. Niki, A. Shvartser, Y. Narukawa, T. Mukai and A. Scherer, *Nat. Mater.*, 2004, **3**, 601.

18 X. Gu, T. Qiu, W. Zhang, P. K. Chu, *Nanoscale Res. Lett.* 2011, **6**, 199.

19 D.-M. Yeh, C.-F. Huang, C.-Y. Chen, Y.-C. Lu and C. C. Yang, *Nanotechnology*, 2008, **19**, 345201.

20 A. Fadil, D. Iida, Y. Chen, J. Ma, Y. Ou, P. M. Petersen and H. Ou, *Sci. Rep.*, 2014, **4**, 6392.

21 M.-K. Kwon, J.-Y. Kim, B.-H. Kim, I.-K. Park, C.-Y. Cho, C. C. Byeon and S.-J. Park, *Adv. Mater.*, 2008, **20**, 1253.

22 S. G. Zhang, X. W. Zhang, Z. G. Yin, J. X. Wang, J. J. Dong, H. L. Gao, F. T. Si, S. S. Sun, and Y. Tao, *Appl. Phys. Lett.*, 2011, **99**, 181116.

23 S. G. Zhang, X. W. Zhang, Z. G. Yin, J. X. Wang, F. T. Si, H. L. Gao, J. J. Dong, and X. Liu, *J. Appl. Phys.*, 2012, **112**, 013112.

24 J. J. Dong, X. W. Zhang, Z. G. Yin, J. X. Wang, S. G. Zhang, F. T. Si, H. L. Gao, and X. Liu, *Appl. Phys. Lett.*, 2012, **100**, 171109.

25 Q. Qiao, C.-X. Shan, J. Zheng, H. Zhu, S.-F. Yu, B.-H. Li, Y. Jia and D.-Z. Shen, *Nanoscale*, 2013, **5**, 513.

26 I. Gontijo, M. Boroditsky, E. Yablonovitch, S. Keller, U. K. Mishra and S. P. DenBaars, *Phys. Rev. B*, 1999, **60**, 11564.

27 A. Neogi, C.-W. Lee, H. O. Everitt, T. Kuroda, A. Tackeuchi and E. Yablonovitch, *Phys. Rev. B*, 2002, **66**, 153305.

28 C.-F. Lu, C.-H. Liao, C.-Y. Chen, C. Hsieh, Y.-W. Kiang and C. C. Yang, *Appl. Phys. Lett.*, 2010, **96**, 261104.

29 L.-W. Jang, D.-W. Jeon, M. Kim, J.-W. Jeon, A. Y. Polyakov, J.-W. Ju, S.-J. Lee, J.-H. Baek, J.-K. Yang and I.-H. Lee, *Adv. Funct. Mater.*, 2012, **22**, 2728.

30 S. Dang, C. Li, W. Jia, Z. Zhang, T. Li, P. Han, and B. Xu, *Opt. Express*, 2012, **20**, 23290.

31 W. Z. Liu, H. Y. Xu, C. L. Wang, L. X. Zhang, C. Zhang, S. Y. Sun, J. G. Ma, X. T. Zhang, J. N. Wang and Y. C. Liu, *Nanoscale*, 2013, **5**, 8634.

32 C. Zhang, C. E. Marvinney, H. Y. Xu, W. Z. Liu, C. L. Wang, L. X. Zhang, J. N. Wang, J. G. Ma and Y. C. Liu, *Nanoscale*, 2015, **7**, 1073.

33 S. A. Maier, *Plasmonics: Fundamentals and Applications*, Springer, 2007.

34 S. Baruah and J. Dutta, *Sci. Technol. Adv. Mater.*, 2009, **10**, 013001.

35 B. Cheng and E. T. Samulski, *Chem. Commun.*, 2004, **8**, 986.

36 H. Mertens, J. Verhoeven, A. Polman and F. D. Tichelaar, *Appl. Phys. Lett.*, 2004, **85**, 1317.

37 T. Hirakawa and P. V. Kamat, *J. Am. Chem. Soc.* 2005, **127**, 3928.

38 M. C. Morris, H. F. McMurdie, E. H. Evans, B. Paretzkin, H. S. Parker, N. C. Panagiotopoulos and C. R. Hubbard, *Standard X-ray Diffraction Powder Patterns: Section 18. Data for 58 Substances*, UNT Digital Library, 1981.

39 G.B. Harris, *Philosophical Magazine*, 1952, **43**, 113.

40 E. Fred Schubert, *Light-Emitting Diodes*, Cambridge University Press, 2006.

41 Y. J. Lee, C. J. Lee, C. H. Chen, T. C. Lu, and H. C. Kuo, *IEEE J. Sel. Top. Quant. Electron.*, 2011, **17**, 985.

42 C. B. Lee, B. S. Kang, A. Benayad, M. J. Lee, S.-E. Ahn, K. H. Kim, G. Stefanovich, Y. Park and I. K. Yoo, *Appl. Phys. Lett.*, 2008, **93**, 042115.

43 J. A. Aranovich, D. Golmayo, A. L. Fahrenbruch and R. H. Bube, *J. Appl. Phys.*, 1980, **51**, 4260.

44 D. Qiao, L. S. Yu, S. S. Lau, J. M. Redwing, J. Y. Lin and H. X. Jiang, *J. Appl. Phys.*, 2000, **87**, 801.